

The iron and oxygen content of LMC Classical Cepheids and its implications for the Extragalactic Distance Scale and Hubble constant[★]

Equivalent Width analysis with Kurucz stellar atmosphere models

Martino Romaniello¹, Adam Riess^{2,3}, Sara Mancino¹, Richard I. Anderson⁴, Wolfram Freudling¹, Rolf-Peter Kudritzki^{5,6}, Lucas Macrì⁷, Alessio Mucciarelli^{8,9}, and Wenlong Yuan³

¹ European Southern Observatory, Karl-Schwarzschild-Strasse 2, D-85478 Garching bei München
e-mail: martino.romaniello@eso.org

² Space Telescope Science Institute, 3700 San Martin Drive, Baltimore, MD 21218, USA

³ Department of Physics and Astronomy, Johns Hopkins University, Baltimore, MD 21218, USA

⁴ Institute of Physics, Laboratory of Astrophysics, École Polytechnique Fédérale del Lausanne (EPFL), Observatoire de Suverny, 1290 Versoix, Switzerland

⁵ LMU München, Universitätssternwarte, Scheinerstrasse 1, D-81679, Germany

⁶ Institute for Astronomy, University of Hawaii at Manoa, 2680 Woodlawn Drive, Honolulu, HI 96822, USA

⁷ Mitchell Institute for Fundamental Physics & Astronomy, Department of Physics & Astronomy, Texas A&M University, College Station, TX 77843, USA

⁸ Dipartimento di Fisica e Astronomia Augusto Righi, Università degli Studi di Bologna, Via Gobetti 93/2, 40129 Bologna, Italy

⁹ INAF – Osservatorio di Astrofisica e Scienza dello Spazio di Bologna, Via Gobetti 93/3, 40129 Bologna, Italy

Received September 15, 1996; accepted March 16, 1997

ABSTRACT

Context. Classical Cepheids are primary distance indicators and a crucial stepping stone to determining the present-day value of the Hubble constant H_0 to the precision and accuracy required to constrain apparent deviations from the Λ CDM Concordance Cosmological Model.

Aims. We have measured the iron and oxygen abundances of a statistically significant sample of 90 Cepheids in the LMC, one of the anchors of the local Distance Scale, quadrupling the prior sample and including 68 of the 70 Cepheids used to constrain H_0 by the SH0ES program. The goal is to constrain the extent to which the Cepheid luminosity is influenced by their chemical composition, which is an important contributor to the uncertainty on the determination of the Hubble Constant itself and a critical factor in the internal consistency of the distance ladder.

Methods. We have derived stellar parameters and chemical abundances from a self-consistent spectroscopic analysis based on Equivalent Width of absorption lines.

Results. The iron distribution of Cepheids in the LMC can be very accurately described by a single Gaussian with a mean $[\text{Fe}/\text{H}] = -0.407 \pm 0.003$ dex and $\sigma = 0.076 \pm 0.003$ dex. The latter is fully compatible with the measurement error and supports the low dispersion of 0.069 mag seen in the NIR *HST* LMC period-luminosity relation. The uniformity of the abundance has the important consequence that the LMC Cepheids alone cannot provide any meaningful constraint on the dependence of the Cepheid Period–Luminosity relation on chemical composition at any wavelength. This revises a prior claim based on a small sample of 22 LMC Cepheids that there was little dependence (or uncertainty) between composition and NIR luminosity, a conclusion which would produce an apparent conflict between anchors of the distance ladder with different mean abundance. The chemical homogeneity of the LMC Cepheid population makes it an ideal environment to calibrate the metallicity dependence between the more metal poor SMC and metal rich Milky Way and NGC 4258.

Key words. Hubble Constant – Cepheid stars – stellar abundances

1. Introduction

The current discrepancy on the present-day value of the Hubble Constant H_0 is arguably one of the most far-reaching open problems in astrophysics today. The extrapolation of early-Universe Cosmic Microwave Background measurements assuming the Λ CDM Cosmological Concordance Model predicts a value of $H_0 = 67.4 \pm 0.5$ km/s/Mpc (Planck Collaboration 2020). The comparison to the best late-Universe local measurement of $H_0 = 73.2 \pm 1.3$ km/s/Mpc (Riess et al. 2021, SH0ES project), which is independent

[★] Based on observations collected at the European Southern Observatory under ESO programmes 66.D-0571 and 106.21ML.003.

from any such assumptions, reveals a significant 4.2σ tension. Moreover, *all* recent local determinations, obtained by different groups with different methods, exceed the early-Universe prediction (e.g. Verde et al. 2019; Riess 2020, and references therein). It is, then, by now almost inescapable to conclude that there indeed is a meaningful difference between early- and local-Universe values of H_0 . This is hugely consequential: in spite of its many phenomenological successes, the Λ CDM model does not, in fact, provide a complete description of the Universe

Classical Cepheids play a pivotal role in this context, since they are primary distance indicators and a crucial stepping stone to determining the present-day value of the Hubble constant to the precision and accuracy required to constrain possible deviations from the Λ CDM. In particular, the SH0ES project has built a clean, three-rung distance ladder based them and on type-Ia Supernovæ. The goal is to measure the local value of the Hubble constant H_0 to an accuracy better than 1%, so as to provide a meaningful match to the early-Universe value derived from the Cosmic Microwave Background.

Cepheids can be used to measure distances because their brightness pulsates according to the Leavitt Law (Leavitt & Pickering 1912) that links the period of such pulsations, which is independent of distance, to their mean magnitude, which scales as the inverse of the distance squared (Period–Luminosity relation, PL). The uncertainty on the behaviour of the PL relation with chemical composition is a major contributor to the overall SH0ES H_0 error budget (0.9% out of 1.8%, Riess et al. 2021). Indeed, recent results using Galactic and Magellanic Cloud Cepheids confirm that, while progress is being made in terms of larger samples, as crucially enabled by GAIA parallaxes, the slope of a potential dependence of the Cepheid luminosity on metal content remains too loosely constrained, with significant differences between different studies, e.g. -0.221 ± 0.051 mag/dex Breuval et al. (2021) vs. -0.456 ± 0.099 mag/dex Ripepi et al. (2021) for the slope in the K_s band.

Here, we provide accurate direct abundance measurements from high-resolution spectroscopy of Cepheids stars in the LMC, one of the three anchor galaxies in the SH0ES distance ladder (Riess et al. 2019). The paper is organised as follows. In section 2 we present the data and their reduction to calibrated 1-dimensional spectra. Section 3 describes the derivation of the stellar parameters that are needed in order to measure chemical abundances. These are discussed in Sections 4 and 5 for iron and oxygen, respectively. Finally, conclusions are drawn in Section 6.

2. Observations and data reduction

We have assembled our sample of 90 Classical Cepheids in the LMC by combining proprietary data for 68 out of the 70 stars that define the SH0ES fiducial PL relation (Riess et al. 2019) with 22 archival spectra observed in the same instrumental setup. For the former ones, this is the first measurement of their chemical composition. Iron abundances for the remaining 22 were already published in Romaniello et al. (2008). Here, we revise those measurement, which we find were affected by an undetected systematics.

All stars are listed in the in the OGLE IV catalogue (Udalski et al. 2015; Soszyński et al. 2015). In the following, we will use the OGLE identifier, shortened for convenience (e.g. OGLE-LMC-CEP-0966 to OGLE0966). Their on-sky distribution and the Period–Luminosity relations in the various bands of the SH0ES sample are presented in Figures 1 and 2, respectively.

We have excluded two of the SH0ES stars from our spectroscopic sample (OGLE1940, OGLE1945; open circles in Figure 2) because they are too faint in the optical to obtain spectra for in a reasonable amount of time. They are also significant outliers from the Period–Luminosity relation in all magnitudes except m_H^W and excluding them from the analysis has no impact on our conclusions.

All 90 stars were observed with the UVES spectrograph at ESO’s VLT telescope in the UVES 580 setting. It covers the wavelength range between 4780 and 6800 Å with a gap between 5760 and 5830 Å. The instrumental resolving power is $R \sim 50,000$, but Cepheids have intrinsically broad spectral lines, yielding an effective value of $R \sim 20,000$. The proprietary observation of the SH0ES sample were carried out in Service Mode, with each star observe once at a random phase during the pulsational cycle. Observing constraints and exposure times were adapted to each star in order to deliver data of uniform quality (signal-to-noise ratios larger than 40). In two cases (OGLE0545, OGLE1647), they were at first executed outside of the constraints we had specified. They were subsequently successfully repeated and we did not use the first set of data, because they did not add significantly to the final quality. No constraints were set on the pulsational phase at the time of observation, which is, then, random. The log of the observations we did use in the analysis is reported in Table 1. We refer the reader to Romaniello et al. (2008) for the details of the observations of the 22 archival Cepheids.

We have downloaded the raw science files from the ESO Science Archive ¹ both for our proprietary data and the archival ones, together with the calibrations provided by the system according to the instrument Calibration Plan (Sbordone & Ledoux 2020). We have reduced the data with the instrument pipeline version 6.1.3 (Møller Larsen, Modigliani & Bramich 2020), executed within the ESOReflex environment (Freudling et al. 2013). We have added a custom step to the default processing cascade to combine repeated observations of the same targets. In all cases, these are taken in sequence (see Table 1), so a simple co-addition of the raw 2D frames serves the purpose.

In the first pass, all data was processed with the default pipeline recipe parameters, which were then optimised by individually inspecting the results. In all cases, we have reduced the rejection threshold during spectral extraction to 5σ (parameter `reduce.extract.kappa` in the `uves_obs_scired` recipe) to limit the impact of cosmic ray hits and detector defects. In the case of star OGLE0936, the trace of bright neighbouring star is clearly visible in the 2D spectrum and the default extraction window includes them both. We have, then, tailored it to only include the star of interest (parameter `reduce.extract.kappa=26` in the `uves_obs_scired` recipe). In all other cases, the default recipe parameter were confirmed to be adequate and were left unchanged.

¹ <http://archive.eso.org>

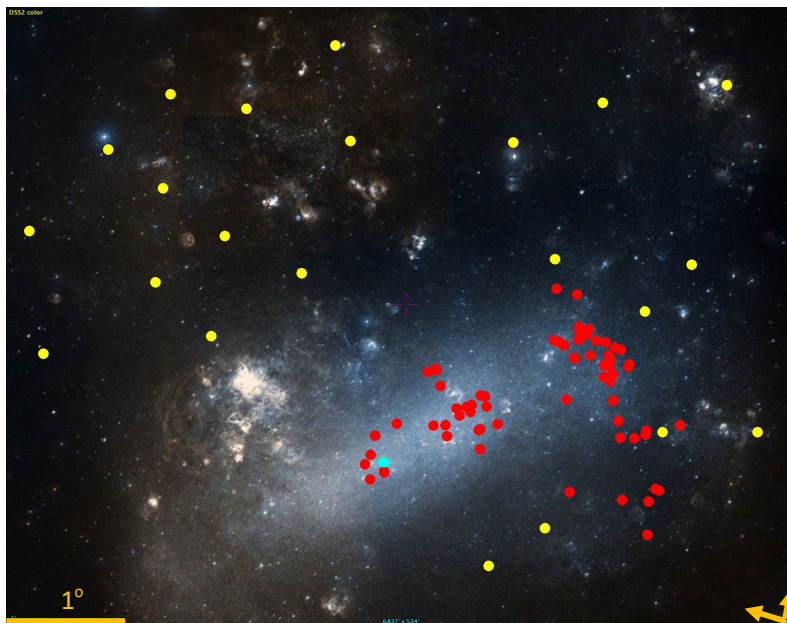


Fig. 1. The distribution on the plane of the sky of the 68 SH0ES Classical Cepheids targeted in this paper (red dots). The 2 for which we do not have spectroscopic data are marked in cyan. The 22 stars from the Romaniello et al. (2008) sample that we have re-analyses here are shown as yellow dots. The figure was generated with the “Aladin sky atlas” software (Boch & Fernique 2014), using a DSS2 color image of the LMC as background.

Table 1. Log of the spectroscopic observations of the 68 SH0ES Cepheids. All stars were observed in the same instrumental setting: UVES 580. Data for OGLE0510 were already available in the ESO Science Archive, so we retrieved it from there and analysed them in the same way as the others. Observations longer than 45 minutes were split in two back-to-back exposures.

Cepheid	Filename timestamp ^a	MJD ^b
OGLE0434	2020-11-07T02:47:44.709	59160.11649
OGLE0434	2020-11-07T02:47:52.206	59160.11658
OGLE0501	2020-10-24T04:50:05.197	59146.20145
OGLE0501	2020-10-24T04:50:13.252	59146.20154
OGLE0512	2020-10-24T05:25:26.486	59146.22600
OGLE0512	2020-10-24T05:25:36.488	59146.22612
OGLE0528	2020-10-09T07:28:41.908	59131.31160
OGLE0528	2020-10-09T07:28:48.852	59131.31168
OGLE0545	2020-11-07T03:00:20.624	59160.12524
OGLE0545	2020-11-07T03:00:29.841	59160.12535
OGLE0510	2000-10-11T04:34:30.713	51828.19063
OGLE0510	2000-10-11T04:44:53.443	51828.19784

Notes.

This table is available in its entirety in machine-readable form.

^(a) The name of the raw science file in the ESO Science Archive is UVES.timestamp.

^(b) MJD = JD - 2,400,000.5.

3. Stellar parameters

3.1. The Equivalent Width method

In order to self-consistently determine the stellar parameters (effective temperature T_{eff} , surface gravity in logarithmic units $\log(g)$ and microturbulent velocity v_{turb}) and chemical abundances, we use the equivalent width (EW) method. Very in brief, for each star, the EWs of iron lines as measured in the observed spectrum are compared to the ones from a stellar atmosphere model for a given set

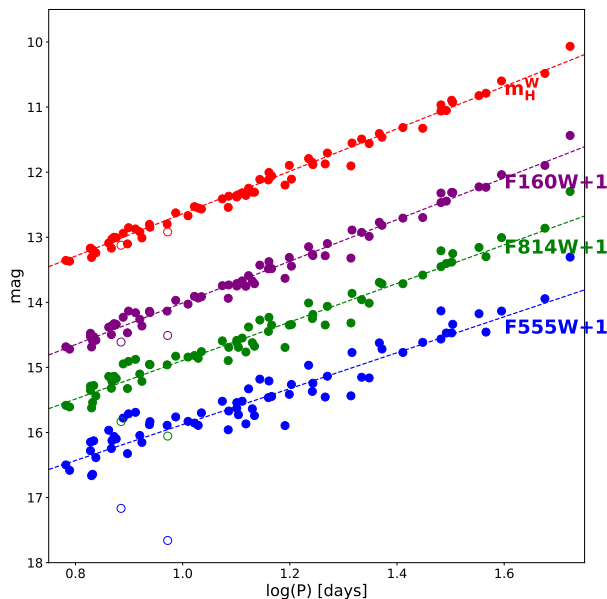


Fig. 2. The Period–Luminosity relations in the various bands of the sky of the SH0ES Classical Cepheids (Riess et al. 2019, see Table 2 and Figure 3). The two for which we do not have spectroscopic data are marked as open circles. The scatter in the m_H^W relation is a mere 0.075 mag, making it the tightest to date.

of stellar parameters to derive the abundances from each individual line. These are, then, iterated upon until convergence is reached when the following conditions are met:

- *Effective temperature* is derived by imposing excitation equilibrium, that is that there be no residual correlation between the iron abundance and the excitation potential χ of the neutral iron lines. As demonstrated, e.g., by Mucciarelli & Bonifacio (2020), above a metallicity of ~ -1.5 , spectroscopic temperature provide an unbiased estimate.
- The best value of *surface gravity* comes from imposing ionization equilibrium method, thus requiring that, for a given species, the abundance is the same within the uncertainties from lines of two different ionization states (typically, neutral and singly ionized lines).
- *Microturbulent velocity* is set by requiring that there is no residual correlation between the iron abundance and the line EW as a measure of the line strength.
- The final *iron abundance* is the mean of the ones from the individual lines in the convergence iteration.
- The initial values of the parameters were set for all stars as follows: $T_{\text{eff}} = 5500$ K, $\log(g) = 1$ cm/s^2 , $[\text{Fe}/\text{H}] = -0.33$ dex and $v_{\text{turb}} = 2.50$ km/s. Changing each of them up to a factor of two influences the resulting abundances randomly at the level of a hundredths of dex.

The abundance of oxygen is, then, measured with the stellar parameters determined as described above.

We have used as input the list of Genovali et al. (2013) for the spectral location of unblended FeI and FeII lines (Table 2). It was compiled specifically for Cepheid stars, thus providing a clean set of lines to avoid as much as possible line crowding for these type of stars that have intrinsically broad features (FWHM \sim 0.2-0.3 Å). We have measured the EWs with the DAOSPEC code (Stetson & Pancino 2008), executed on our entire sample of stars by the 4DAO software (Mucciarelli 2013).

In our analysis, we have adopted the GALA implementation of the EW method, which was extensively and specifically tested on UVES data (Mucciarelli et al. 2013). As input physics, we have used the classical grid of ATLAS9 LTE stellar atmosphere models (Castelli & Kurucz 2004). During the analysis, for each spectrum lines are rejected from the fit based on a number of quality criteria, so that the final set of lines used in the analysis varies among the spectra, depending on circumstances like, e.g. signal-to-noise and depth of the line. In all cases, though, a large enough number is retained, so that the resulting solution is meaningful in terms of stellar parameters and elemental abundances. This is shown in Figure 3, where the number of lines actually used in the analysis for each spectrum is shown.

Once convergence is reached, the uncertainty on the elemental abundance is computed, taking into account the covariance among the stellar parameters according to the prescription of Cayrel et al. (2004).

In order to gauge the quality of the results, in Figure 4 we plot the distributions of the quantities that are minimised when computing the stellar parameters: slope S_χ of FeI abundance vs excitation potential χ for T_{eff} , the slope S_{EWR} of the relation between FeI abundance and reduced Equivalent Width $\text{EWR} = \log(\text{EW}/\lambda)$ for v_{turb} and the difference between FeI and FeII for $\log(g)$. In order to interpret the residuals in the convergence criteria in terms of their impact on the final abundance determination,

Table 2. List of the 189 FeI, 28 FeII and 2 OI lines used as input in the analysis. From left to right the columns display wavelength, ion identification, oscillator strength $\log(gf)$ and excitation potential EP values (adapted from Genovali et al. 2013, with updated values from the Kurucz/Castelli database^a). As part of the abundance analysis, individual lines may be rejected based on the criteria detailed in Section 3.1. The distributions of the lines retained in the analysis are shown as histograms in Figure 3.

λ [Å]	Ion	$\log(gf)^a$	EP [eV] ^a
4892.86	FeI	-0.876	4.22
4893.81	FeII	-4.157	2.83
4917.23	FeI	-1.160	4.19
4923.92	FeII	-1.559	2.89
4924.77	FeI	-2.114	2.28
4932.08	FeI	-1.483	4.65
4950.10	FeI	-1.500	3.42
4973.10	FeI	-0.690	3.96
4993.35	FeII	-3.684	2.81
4994.13	FeI	-3.080	0.92
...

Notes.

This table is available in its entirety in machine-readable form.

^(a) <https://wwwuser.oats.inaf.it/castelli/linelists.html>

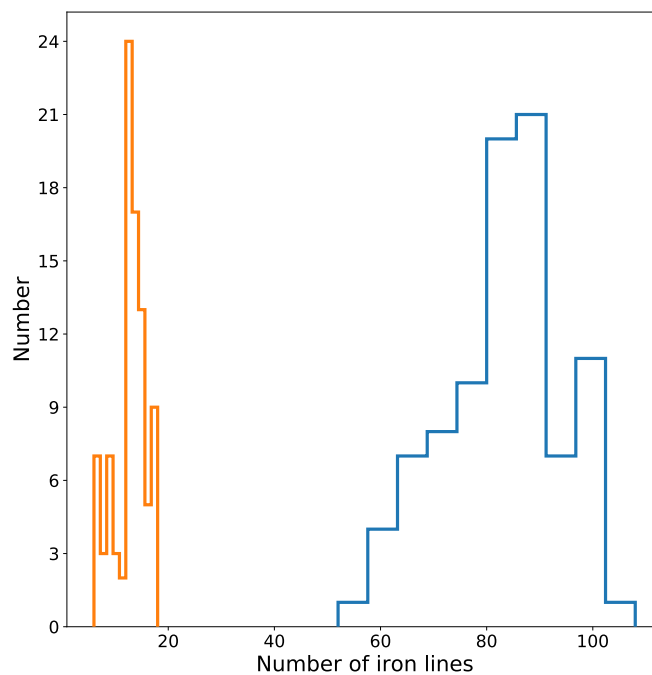


Fig. 3. The number of FeI (blue histogram) and FeII (orange histogram) spectral lines retained in the abundance analysis of each of the 90 programme stars after outlier rejection as part of the fitting procedure with the GALA code (see Section 3.1). The full input line list is reported in Table 2.

which is our ultimate goal, in panels (a) and (b) of the same Figure we plot also the corresponding peak-to-peak values of the spread in iron abundance, computed for every star as:

$$\Delta A(\text{FeI})_{\text{p2p}} = \text{slope} \times \text{lever} \quad (1)$$

where $\text{slope} = S_{\chi}$ or S_{EWR} and lever is the range spanned in χ and EWR, respectively, by the lines ultimately used in the fit. In other words, these peak-to-peak values are the maximum scatter in the abundance introduced by residual correlations in the minimisation process. As it can be seen, their impact is of the order of a mere few hundredths of dex at maximum. The same applies when considering the iron abundances of the 90 stars versus the stellar parameters that, as shown in Figure 5, do not show any appreciable residual trend (the expectation being, of course, that the chemical composition of a Cepheid does not depend on its stellar parameters along its crossings of the instability strip).

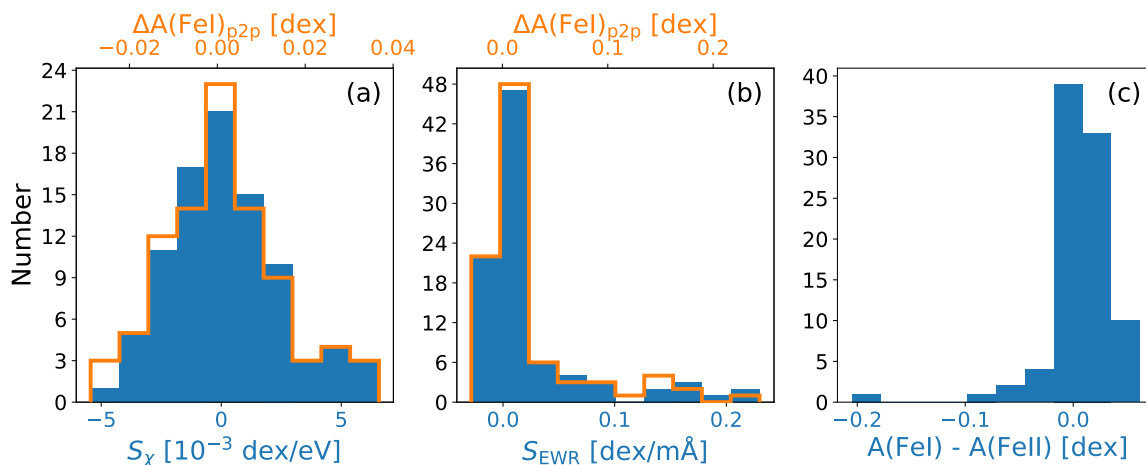


Fig. 4. Histograms of the output values of the diagnostics used to derive the stellar parameters for the 90 stars in our combined sample. *Panel (a):* slope S_χ of FeI abundance vs excitation potential χ used to derive the effective temperature T_{eff} (solid blue curve, bottom x scale). The corresponding peak-to-peak values of the spread in iron abundance ($\Delta A(\text{FeI})_{\text{p2p}}$, see Equation (1)) is plotted as open orange curve (top x scale). *Panel (b):* slope S_{EWR} of the relation between FeI abundance and reduced EW $\text{EWR} = \log(\text{EW}/\lambda)$, which ranges between -5.5 and -4.5 , and used to constrain the microturbulent velocity v_{turb} (solid blue curve, bottom x scale). Also here, the corresponding peak-to-peak values of the spread in iron abundance ($\Delta A(\text{FeI})_{\text{p2p}}$, see Equation (1)) is plotted as open orange curve (top x scale). *Panel (c):* the difference between FeI and FeII, the minimization of which is used to determine the surface gravity $\log(g)$. The mean and standard deviation of the distribution are 0.007 and 0.033 dex, respectively, indicating an excellent agreement between the derived FeI and FeII abundances, and hence gravity, with no appreciable systematics.

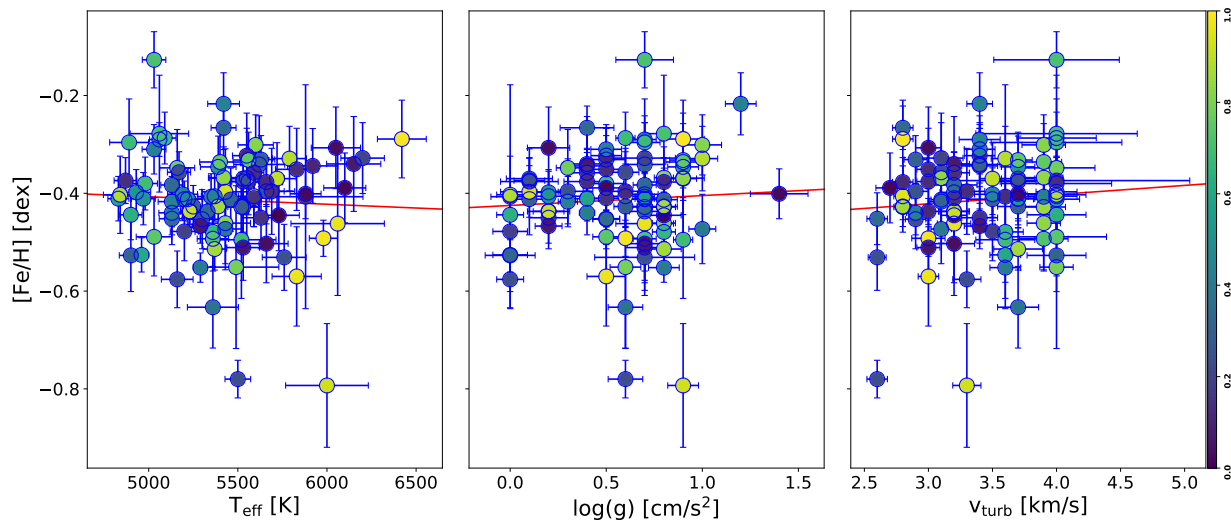


Fig. 5. The measured iron abundance vs the stellar parameters simultaneously derived in the GALA analysis. As expected, hardly any residual trend is present (red line). The points are color-coded according to the phase along the pulsational cycle the stars were observed at, with the scale represented by the bar on the far right.

The derived stellar parameters are reported in Table 3 for the SH0ES sample and in Table 4 for the archival one.

In order to make our analysis reproducible, in Appendix A and B we provide, respectively, the full GALA configuration file we have used and the EWs of the individual lines for each star.

3.2. Stellar vs pulsational parameters

The fact that Cepheids pulsate according to well defined laws allows to perform additional consistency checks on the stellar parameters derived in the abundance analysis. To this end, in Figure 6 we plot them as a function of pulsational period. As it can be seen, the iron abundance shows a negligible correlation with the period, as expected from it being an intrinsic property of the star independent from the pulsation mechanism. For the stellar parameters, on the other hand, correlations are present. This is also expected, in that they reflect the location of the stars in the instability strip when they were observed. The scatter is dominated by having caught the stars at a random phase along the pulsational cycle.

Figure 7 displays the correlation of temperature with the phase along the pulsation cycle each star was observed at. As expected, the stars are coldest towards the middle of the pulsation cycle and get hotter at either extreme, with an excursion of about $1,000$ K. All of these diagnostics further confirm the soundness and robustness of our analysis.

Table 3. Stellar parameters as derived in the abundance analysis for the SH0ES sample.

CEP	T_{eff}	dT_{eff}	$\log(g)$	$d\log(g)$	v_{turb}	dv_{turb}	Phase
OGLE0434	5660	100	0.30	0.13	2.90	0.10	0.2577
OGLE0501	5130	77	0.30	0.05	3.10	0.09	0.4385
OGLE0510	5530	64	0.10	0.15	3.70	0.14	0.1274
OGLE0512	5200	79	0.00	0.09	3.50	0.15	0.1892
OGLE0528	5200	64	0.10	0.08	3.50	0.19	0.3005
OGLE0545	5420	85	0.80	0.05	3.90	0.15	0.8352
OGLE0590	5880	322	0.00	0.10	3.60	0.09	0.1314
OGLE0594	5520	194	0.90	0.05	3.60	0.23	0.6911
OGLE0648	5300	90	0.50	0.07	2.90	0.08	0.2372
OGLE0683	5560	105	0.40	0.12	3.00	0.09	0.1281
...

Notes.

This table is available in its entirety in machine-readable form.

Table 4. Stellar parameters as re-derived here in the abundance analysis for the Romaniello et al. (2008) sample.

CEP	T_{eff}	dT_{eff}	$\log(g)$	$d\log(g)$	v_{turb}	dv_{turb}	Phase
OGLE107	5390	42	0.80	0.07	2.80	0.06	0.860
OGLE461	4890	109	0.70	0.08	4.00	0.51	0.682
OGLE510	5530	67	0.10	0.12	3.70	0.13	0.256
OGLE655	5590	86	0.50	0.11	3.20	0.11	0.144
OGLE945	4960	40	0.00	0.09	3.60	0.12	0.605
OGLE1100	6200	122	0.70	0.16	3.10	0.17	0.201
OGLE1128	5370	65	0.80	0.09	3.70	0.19	0.861
OGLE1290	4870	64	0.10	0.08	4.00	1.04	0.136
OGLE1327	5660	122	0.70	0.09	3.20	0.16	0.037
OGLE2337	5590	56	0.40	0.09	3.20	0.12	0.130
...

Notes.

This table is available in its entirety in machine-readable form.

4. Iron abundances

Because of the large number of available lines in the optical spectral region, iron is often used as a proxy for the overall metal content and as a reference against which other elemental abundances are measured. The FeI and FeII abundances derived from the procedure described above are listed in Tables 5 and 6. In the following, unless otherwise noted, when talking about abundances we will refer to FeI simply as iron.

In Figure 8, we show the histogram of the iron values for our 90 stars. Fitting it with a Gaussian yields a mean value of -0.407 ± 0.003 dex, with a width $\sigma = 0.076 \pm 0.003$ dex (the values of straight mean and standard deviation are -0.41 and 0.09 , respectively). The latter is practically indistinguishable from the mean error as propagated through the abundance analysis (~ 0.07 dex, green dashed vertical lines), making the distribution consistent with a single abundance as broadened by the observational uncertainties.

4.1. Comparison with previous results

The most direct comparison with our results is with those presented by Romaniello et al. (2008). The main difference between the analyses is that here we derive the stellar effective temperature together with the other parameters (see section 3.1), while Romaniello et al. (2008) first fix the temperature using the Line Depth Ratio method (LDR, specifically in the implementation of Kovtyukh & Gorlova 2000), then derive the remaining parameters $\log(g)$ and v_{turb} , and the iron abundance.

In the left panel of Figure 10, we plot the histogram of the iron abundances from Table 9 of Romaniello et al. (2008), together with a Gaussian fit to it. The mean value of the distribution is -0.30 ± 0.02 dex with $\sigma = 0.13 \pm 0.02$ dex, to be compared to -0.4 and 0.07 dex, respectively, for our 90 stars (see Section 4 above).

The results of the present analysis on the Romaniello et al. (2008) sample are shown in the right panel of Figure 10. With a measured Gaussian mean of -0.43 ± 0.01 and $\sigma = 0.08 \pm 0.01$ dex, the ensemble properties of the reanalysed Romaniello et al. (2008) sample compare very well with those of the 90 stars of the combined sample, as well as to the 68 SH0ES stars alone

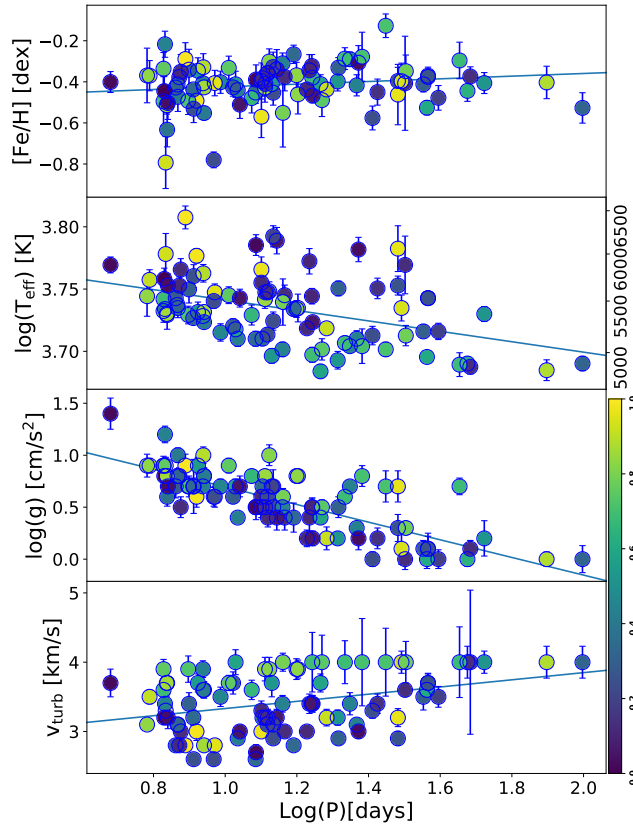


Fig. 6. The stellar parameters as measured in our analysis vs the stars' pulsational periods. The iron abundance shows a negligible correlation with the period, further confirming the robustness of the analysis. The other stellar parameters, on the other hand, the correlations reflect the location of the instability strip, with a scatter dominated by having observed the stars at a random phase in the pulsational cycle. The points are color-coded according to the phase along the pulsational cycle the stars were observed at, with the scale represented by the bar on the far right.

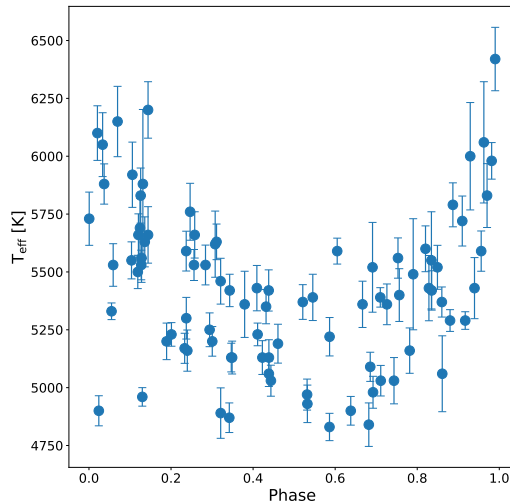


Fig. 7. The derived stellar effective temperature (T_{eff}) as a function of the phase along the pulsational cycle each star was observed at (see Table 3). The size of the mean error on T_{eff} is shown by the errorbar in the lower-left corner.

(mean = -0.399 ± 0.003 dex, $\sigma = 0.0720.003$ dex). This rules out actual differences between the samples and points to differences in the abundance analysis, instead.

The discrepancy in the mean iron abundance between the one we have derived here and the one in Romaniello et al. (2008) can be traced back to an offset of about 170 K in the temperatures as computed with the two methods, the present re-analysis yielding

Table 5. Stellar iron abundances for the SH0ES sample.

CEP	FeI				FeII			
	Abundance ^a	Dispersion ^b	Uncertainty ^c	N _{lines}	Abundance ^a	Dispersion ^b	Uncertainty ^c	N _{lines}
OGLE0434	-0.40	0.12	0.07	101	-0.43	0.13	0.04	15
OGLE0501	-0.42	0.09	0.05	84	-0.43	0.06	0.03	12
OGLE0510	-0.38	0.11	0.03	82	-0.39	0.14	0.03	9
OGLE0512	-0.48	0.13	0.06	91	-0.41	0.11	0.01	14
OGLE0528	-0.41	0.12	0.04	91	-0.43	0.07	0.02	15
OGLE0545	-0.37	0.09	0.06	78	-0.40	0.04	0.05	10
OGLE0590	-0.41	0.10	0.23	83	-0.38	0.13	0.08	15
OGLE0594	-0.49	0.14	0.12	71	-0.50	0.02	0.10	6
OGLE0648	-0.45	0.09	0.06	98	-0.47	0.09	0.04	17
OGLE0683	-0.38	0.11	0.07	90	-0.40	0.14	0.05	16
...

Notes.

This table is available in its entirety in machine-readable form.

Unless otherwise noted, in the following we will refer to the FeI abundance simply as iron.

^(a) Logarithmic abundance with respect to hydrogen, in solar units: $[\text{Fe}/\text{H}] \equiv A(\text{Fe})_{\text{star}} - A(\text{Fe})_{\odot}$, where $A(\text{Fe}) = \log(N_{\text{Fe}}/N_{\text{H}}) + 12$ and we adopt $A(\text{Fe})_{\odot} = 7.50$ from Asplund et al. (2009).

^(b) Standard deviation of the individual line measurements.

^(c) Uncertainty in the abundance determination according to Cayrel et al. (2004), which includes the effects of covariance among the stellar parameters.

Table 6. Stellar iron abundances from the re-analysis of the Romaniello et al. (2008) sample.

CEP	FeI				FeII			
	Abundance ^a	Dispersion ^b	Uncertainty ^c	N _{lines}	Abundance ^a	Dispersion ^b	Uncertainty ^c	N _{lines}
OGLE107	-0.43	0.09	0.03	101	-0.46	0.09	0.04	17
OGLE461	-0.30	0.15	0.09	65	-0.30	0.08	0.10	9
OGLE510	-0.37	0.10	0.04	83	-0.43	0.14	0.03	10
OGLE655	-0.41	0.11	0.06	94	-0.43	0.14	0.05	17
OGLE945	-0.53	0.09	0.04	83	-0.47	0.09	0.00	14
OGLE1100	-0.33	0.12	0.07	79	-0.35	0.19	0.04	18
OGLE1128	-0.51	0.12	0.04	82	-0.51	0.10	0.05	13
OGLE1290	-0.37	0.13	0.05	59	-0.36	0.07	0.04	7
OGLE1327	-0.50	0.15	0.08	81	-0.52	0.10	0.06	13
OGLE2337	-0.36	0.09	0.04	87	-0.36	0.11	0.04	15
...

Notes.

This table is available in its entirety in machine-readable form.

Unless otherwise noted, in the following we will refer to the FeI abundance simply as iron.

^(a) Logarithmic abundance with respect to hydrogen, in solar units: $[\text{Fe}/\text{H}] \equiv A(\text{Fe})_{\text{star}} - A(\text{Fe})_{\odot}$, where $A(\text{Fe}) = \log(N_{\text{Fe}}/N_{\text{H}}) + 12$ and we adopt $A(\text{Fe})_{\odot} = 7.50$ from Asplund et al. (2009).

^(b) Standard deviation of the individual line measurements.

^(c) Uncertainty in the abundance determination according to Cayrel et al. (2004), which includes the effects of covariance among the stellar parameters.

the lower values. The observed difference in iron is, then, consistent, with the expectation that an increase in temperature of 100 K, at fixed v_{turb} and $\log(g)$, results in an increase in $[\text{Fe}/\text{H}]$ of about 0.07 dex (Romaniello et al. 2008).

As for the difference in dispersion, it can be explained by noticing from Table 9 in Romaniello et al. (2008) that their analysis leaves a significant residual slope between iron abundance and stellar microturbulent velocity (see Figure 9). Once this is removed, for example with a simple linear regression, the remaining scatter is fully compatible with the quoted uncertainty in their measured iron abundances of “typically 0.08-0.1 dex”. Furthermore, in the re-analysis of the spectra, there are no significant residual trends, as it is the case for the whole sample and is illustrated in Figure 5. We, then, confirm that the observed spread in iron abundances among the stars is fully compatible with a measurement uncertainty of ~ 0.07 dex, without additional sources of broadening.

Finally, we note that our results compare very well with those in Urbaneja et al. (2017), who found a mean abundance of $[\text{Fe}/\text{H}] = -0.34 \pm 0.11$ for 23 LMC Blue Supergiant Stars. These are a different, but coeval, type of stars to Cepheids and were analysed with a method than is completely independent from the one we have used here, also incorporating non-LTE effects. The remarkable agreement in iron content between the two samples indicates that the effects of systematics in our analysis, including from possible departures from LTE, are smaller than 0.1 dex.

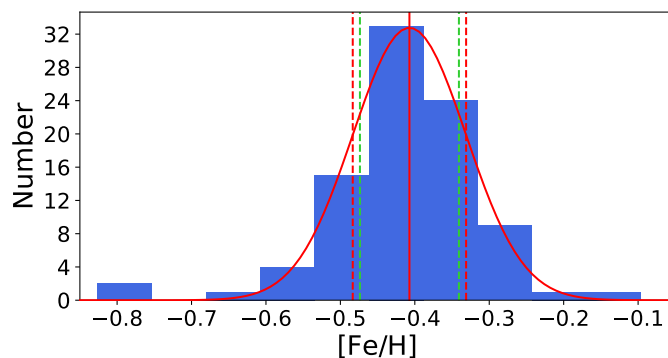


Fig. 8. Histogram of the iron abundances measured for the combined sample of 68 + 22 LMC Cepheids, together with its best fitting Gaussian (solid red curve). The vertical lines mark the position of the peak of the Gaussian ($[\text{Fe}/\text{H}] = -0.407 \pm 0.003$, solid red), plus and minus one Gaussian sigma ($\sigma = 0.076 \pm 0.003$, red dashed) and the mean of the error on the iron abundance resulting from the spectral analysis (~ 0.07 dex, green dashed line, Tables 5 and 6).

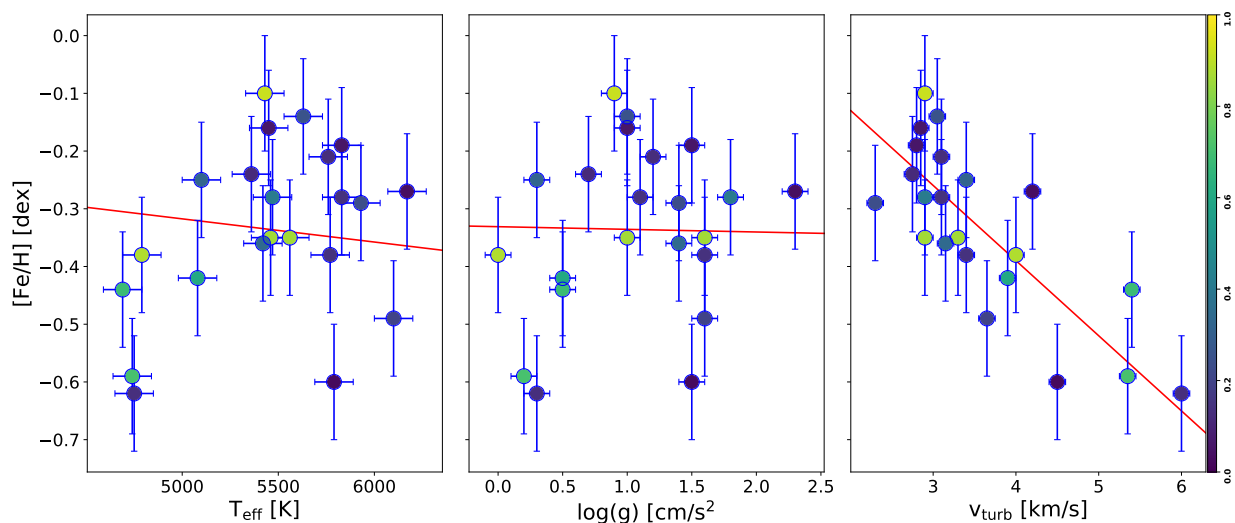


Fig. 9. The measured iron abundance vs the stellar parameters as derived in Romaniello et al. (2008), together with the results of a linear regression (red lines). A clear residual trend is present with v_{turb} , which is responsible for the large scatter of $\sigma = 0.13$ that our analysis does not confirm. The points are color-coded according to the phase along the pulsational cycle the stars were observed at, with the scale represented by the bar on the far right.

4.2. Implications for the Period–Luminosity relation and the distance scale

The 90 LMC Cepheids we have analysed here were not selected in any particular way with respect to their iron content, which was, in fact, not known at all before their spectra were taken. The fact they do not show any appreciable deviation from a Gaussian with a width dictated by the rather stringent measurement uncertainty of ~ 0.08 dex (see Figure 8), together with the fact that they are distributed all over the extent of the LMC (see Figure 1), is indicative that it is a general property of the LMC Cepheids as a population to have the same iron abundance within that limit.

The iron content, then, does not add to the scatter of the LMC Period–Luminosity relation, which is advantageous when used as a tool to measure distances. On the other hand, though, it also means that Cepheids in the LMC alone cannot be used to determine the extent to which the relation itself depends on the chemical composition, the uncertainty on which is an important contributor to the total error budget when determining H_0 (0.9% out of 1.8%, Riess et al. 2021). This is illustrated in the right panel of Figure 11, where it is apparent that the span of iron abundances is too small with respect to the size of the measurement errors to determine any meaningful dependence on that the magnitude residuals in the Wesenheit magnitude m_{H}^{W} with respect to the fiducial Period–Luminosity relation of Riess et al. (2019). For comparison we show a line for no dependence and a ~ -0.2 mag/dex dependence as found by other measurements from gradients within spiral galaxies or between galaxies with difference abundances (e.g., Riess et al. 2019; Breuval et al. 2021; Rijspepi et al. 2021). Because of the large uncertainties on both axes, any attempt to measure a dependence from this data must take care to include both in a fit. This is inherently method-dependent for the reason that it is not well-constrained by the data and we quote illustrative results from two approaches, $\gamma = -0.68 \pm 0.34$ with the *fitexy* algorithm described in Press & Teukolsky (1992), or -0.11 ± 1.3 from a non-linear least-squares from a Monte-Carlo Markov Chain (Imfit).

We also revisit whether γ may be derived from the original Romaniello et al. (2008) sample of 22 LMC Cepheids and their revised values here as shown in Figure 11 with important consequences for the determination of H_0 . It is apparent from Figure 11

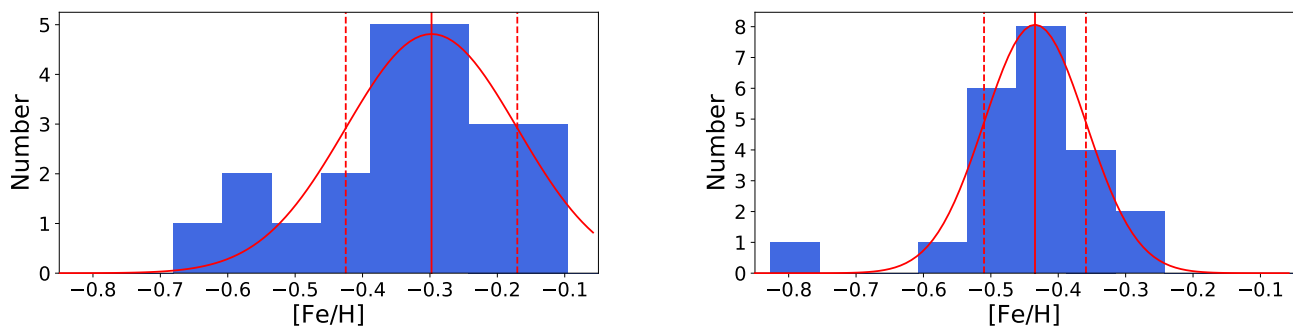


Fig. 10. *Left panel:* histogram of the iron abundances of the the sample of 22 LMC Cepheids in Romaniello et al. (2008, see their Table 9), together with the best fitting Gaussian (solid red curve). The vertical lines mark the position of the peak of the Gaussian (solid red) and plus and minus one Gaussian sigma (red dashed). *Right panel:* same as the left panel, but for our re-analysis of the same spectra. The distribution in the left panel was artificially broadened because of a spurious trend in $[\text{Fe}/\text{H}]$ vs. v_{turb} resulting from the abundance analysis (see Figure 9 and the text).

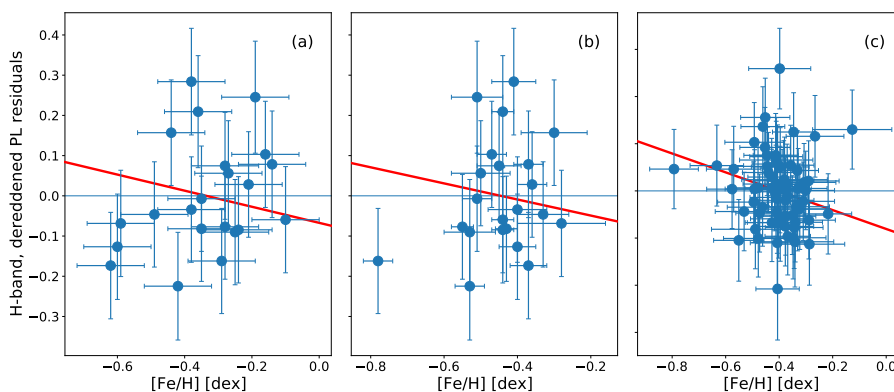


Fig. 11. Residuals in the H-band dereddened magnitude PL relation as a function of iron abundance. *Panel (a):* the original Romaniello et al. (2008) sample of 22 LMC Cepheids, with photometry from Persson et al. (2004). *Panel (b):* the same sample, but with the iron abundances as revised here. *Panel (c):* the SHOES sample of 68 LMC Cepheids, with iron abundances as measured here and photometry from Riess et al. (2019). To guide the eye, in all panels, the red line indicates a metallicity dependence of the Cepheid PL of $\gamma = -0.2$ mag/dex, which is often quoted in the recent literature (e.g., Riess et al. 2019; Breuval et al. 2021; Ripepi et al. 2021).

that the measurement errors in both axes from the earlier, smaller sample are too large (and the span of $[\text{Fe}/\text{H}]$ too small) to usefully constrain γ , with even the more optimistic *fitexy* algorithm giving $\sigma_\gamma > 0.4$ mag/dex for either sample. We cannot reproduce the results of a very strong constraint of a minimal dependence of $\gamma = 0.05 \pm 0.02$ for the *H*-band and $\gamma = 0.02 \pm 0.03$ for the *K*-band given by Freedman & Madore (2011) from the original Romaniello et al. (2008) sample which would be more than 20 times better than what we find achievable. Not only is a small value and uncertainty in γ not supported by the small range of $[\text{Fe}/\text{H}]$ within the LMC, these low values and uncertainties are inconsistent with the value of $\sim -0.22 \pm 0.05$ mag/dex dependence in this region of the NIR found by (e.g., Breuval et al. 2021) by comparing Cepheids between the LMC, SMC and MW to their geometric distances. Other hosts with a broader range of $[\text{Fe}/\text{H}]$ can be used to measure γ internally. This is even possible within the MW using Gaia EDR3 Cepheid parallaxes, where Riess et al. (2021) found $\gamma = -0.20 \pm 0.12$. While comparing hosts with different mean abundance and independent geometric distances reveals a significant metallicity dependence, setting $\gamma = 0$ would likewise cause the appearance of tension between the geometric anchors with difference mean abundance as claimed by Efstathiou (2020)². Therefore, the *inability* to constrain γ within the LMC Cepheid sample is an important conclusion in the context of determining the value of H_0 .

Such a narrow distribution in iron content across the surface of the LMC also implies that virtually no chemical enrichment took place in the look-back time covered by our sample. In order to quantify this, we have converted the Cepheid pulsational periods into stellar evolutionary ages according to the relations by De Somma et al. (2021). The resulting distributions are shown in Figure 12 for two assumptions on the amount of core convective overshooting during the core H-burning stage. Either way, the time span is of the order of 50 Myrs.

5. Oxygen abundances

Oxygen is the third most abundant element in the Universe, after hydrogen and helium and the most abundant one among those not created in the Big Bang. It is also fairly easy to detect and measure as strong emission lines in HII regions in galaxies along the SHOES distance ladder to H_0 and it is, therefore, often used as proxy for the global metallicity (e.g., Riess et al. 2016). However,

² Though Efstathiou (2020) noted “the discrepancy may be attributable to a metallicity dependence of the PL relation” which appears likely.

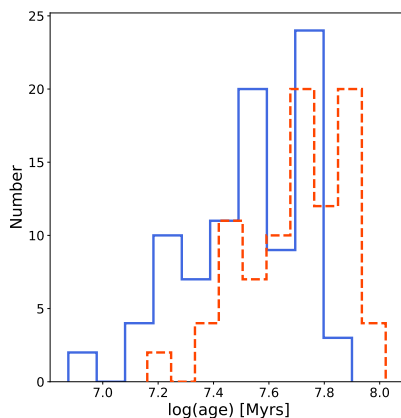


Fig. 12. Age distribution of our programme stars derived by applying the Period–Age relations by De Somma et al. (2021) for two assumptions on the amount of core convective overshooting during the core H-burning stage: no extension above the canonical value predicted by the Schwarzschild criterion (canonical scenario, solid blue line), or a moderate core overshoot (non-canonical scenario, dashed red line).

Table 7. Stellar oxygen abundances for the SH0ES sample.

CEP	OI		
	Abundance ^a	Uncertainty ^b	N _{lines} ^c
OGLE0434	-0.36	0.10	2
OGLE0501	-0.21	0.10	2
OGLE0510	-0.30	0.06	1
OGLE0512	-0.35	0.06	2
OGLE0528	-0.29	0.07	2
OGLE0545	-0.22	0.10	1
OGLE0590	—	—	—
OGLE0594	-0.12	0.21	1
OGLE0648	-0.32	0.11	1
OGLE0683	-0.28	0.12	1
...

Notes.

This table is available in its entirety in machine-readable form.

^(b) Logarithmic abundance with respect to hydrogen, in solar units: $[O/H] \equiv A(O)_{\text{star}} - A(O)_{\odot}$, where $A(O) = \log(N_O/N_H) + 12$ and we adopt $A(O)_{\odot} = 8.69$ from Asplund et al. (2009).

^(b) Uncertainty in the abundance determination according to Cayrel et al. (2004), which includes the effects of covariance among the stellar parameters.

^(c) No oxygen abundance is reported in case no lines could be measured, either because the Equivalent Width of lines could not be measured, or because convergence was not reached in deriving the abundance (26 out of 68 stars).

gas-phase measurements are only a proxy for the stellar ones and may not give consistent results (e.g. Kewley & Ellison 2008; Davies et al. 2017). It is, therefore, important to provide direct measurements on the Cepheids themselves.

Our instrumental setup, however, includes only very few oxygen lines to measure the abundance from, which makes the determination rather more uncertain than iron. Specifically, we have used the two forbidden [OI] lines at 6300.30 and 6363.77 Å to measure the oxygen abundances for our stars³. The results are listed in Tables 7 and 8. For 28 out of 90 stars we could not measure a meaningful oxygen abundance, either because the Equivalent Width of lines could not be measured, or because convergence was not reached in deriving the abundance.

The distribution of the measured oxygen abundances is shown in Figure 13. The mean value from a Gaussian fit is $[O/H] = -0.29 \pm 0.02$ dex with a width of $\sigma = 0.12 \pm 0.02$ dex, consistent with the mean measurement error of 0.11 dex. Therefore, the same consideration of Section 4.2 on the unsuitability of LMC Cepheids alone to constrain the dependence of the PL relation on iron content apply to oxygen, as well.

³ Both transitions cause strong airglow emissions in the night sky. However, at the spectral resolution of UVES, the heliocentric velocity and the radial velocity of the LMC of about 250 km/s shifts them sufficiently away from their rest-frame position so that the measurement is not affected by residuals in the sky subtraction.

Table 8. Stellar oxygen abundances from the re-analysis of the Romaniello et al. (2008) sample.

CEP	OI		
	Abundance ^a	Uncertainty ^b	N _{lines} ^c
OGLE107	-0.33	0.06	2
OGLE461	0.03	0.18	2
OGLE510	-0.30	0.09	1
OGLE655	-0.28	0.10	1
OGLE945	-0.38	0.03	2
OGLE1100	0.02	0.10	2
OGLE1128	-0.33	0.09	1
OGLE1290	-0.29	0.07	1
OGLE1327	-0.17	0.12	1
OGLE2337	-0.33	0.07	1
...

Notes.

This table is available in its entirety in machine-readable form.

^(b) Logarithmic abundance with respect to hydrogen, in solar units: $[O/H] \equiv A(O)_{\text{star}} - A(O)_{\odot}$, where $A(O) = \log(N_O/N_H) + 12$ and we adopt $A(O)_{\odot} = 8.69$ from Asplund et al. (2009).

^(b) Uncertainty in the abundance determination according to Cayrel et al. (2004), which includes the effects of covariance among the stellar parameters.

^(c) No oxygen abundance is reported in case no lines could be measured, either because the Equivalent Width of lines could not be measured, or because convergence was not reached in deriving the abundance (26 out of 68 stars).

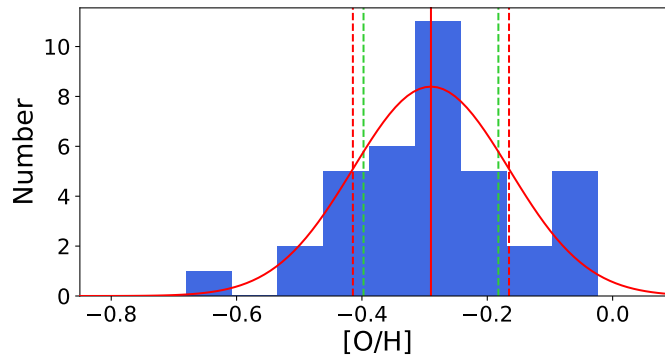


Fig. 13. Histogram of the oxygen abundances measured for the 42 LMC Cepheids out of 68 (see Table 7), together with its best fitting Gaussian (solid red curve). The vertical lines mark the position of the peak of the Gaussian (solid red), plus and minus one Gaussian sigma (red dashed) and the mean of the error on the iron abundance resulting from the spectral analysis (green dashed, Table 7).

6. Summary and conclusions

In this paper, we have analysed the spectra of 90 LMC Cepheids to measure their iron and oxygen abundance. This is of crucial relevance for the local Distance Scale, of which the LMC is one of the anchors.

Our analysis indicates that the iron distribution of Cepheids in the LMC can be very accurately described by a single Gaussian with mean $= -0.407 \pm 0.003$ dex and $\sigma = 0.076 \pm 0.003$ dex for iron and $[O/H] = -0.29 \pm 0.02$ dex with a width of $\sigma = 0.12 \pm 0.02$ dex for oxygen. In both cases the observed scatter is fully compatible with the measurement error. Going beyond the present accuracy in order to characterise the chemical properties of LMC Cepheids will require a very significant effort and may not be worth the while.

Our findings do not support the earlier results by Romaniello et al. (2008), who found a significantly larger distribution in iron ($\sigma = 0.13 \pm 0.02$ dex). The difference can be explained by a residual spurious trend of the iron abundance vs. the microturbulent velocity in their analysis. The difference of 0.1 dex in the mean values of iron can be explained by the different temperature scales. Here we derive the temperatures simultaneously with the other stellar parameters and abundances, while Romaniello et al. (2008) compute them a priori with the Line Depth Ratio method, also on the spectra themselves.

The fact that the chemical abundance distribution is effectively unresolved given the observational uncertainties that are attainable in practice implies that the LMC alone cannot be used to constrain the possible dependency of the Cepheid luminosity on their chemical composition, which is a source of major uncertainty in measuring the Hubble constant to $\sim 1\%$, as required to constrain possible deviations from the Λ CDM Cosmological Concordance Model. The most promising way to do so seems to be combining the LMC with the SMC and the Galaxy, so as to achieve a long enough baseline in abundance with respect to the typical uncertainties.

On the other hand, this extreme chemical homogeneity of the LMC Cepheid population makes it an ideal environment to calibrate the Period–Luminosity relation at this particular metallicity. In retrospect, it is a crucial factor in the finding by the SH0ES

team that the Period–Wesenheit relation in the HST-WFC3 H, V and I bands has a very low intrinsic scatter of a mere 0.075 mag, or 3% (Riess et al. 2019).

Acknowledgements. We warmly thank ESO’s Observing Programme Office and User Support Department for adapting the scheduling of our observations to the evolving constraints dictated by the Covid-19 pandemic. The outstanding job of the staff of ESO’s Paranal Science Operations in carrying out the observations under the gruelling circumstances is gratefully acknowledged. We thank Giulia De Somma, Marcella Marconi and Vincenzo Ripepi for fruitful discussions. SM and RPK acknowledge support by the Munich Excellence Cluster Origins funded by the Deutsche Forschungsgemeinschaft (DFG, German Research Foundation) under Germany’s Excellence Strategy EXC-2094 390783311. RIA acknowledges support from the Swiss National Science Foundation (SNSF) through an Eccellenza Professorial Fellowship (award PCEFP2_194638) as well as from the European Research Council (ERC) under the European Union’s Horizon 2020 research and innovation programme (Grant Agreement No. 947660). This research has made use of “Aladin sky atlas” developed at CDS, Strasbourg Observatory, France.

References

- Asplund, M., Grevesse, N., Sauval, A. J., et al. 2009, *ARA&A*, 47, 481. doi:10.1146/annurev.astro.46.060407.145222
- Boch, T. & Fernique, P. 2014, *Astronomical Data Analysis Software and Systems XXIII*, 485, 277
- Breival, L., Kervella, P., Wielgórski, P., et al. 2021, *ApJ*, 913, 38. doi:10.3847/1538-4357/abf0ae
- Castelli, F., & Kurucz, R. L. 2004, arXiv:astro-ph/0405087.
- Cayrel, R., Depagne, E., Spite, M., et al. 2004, *A&A*, 416, 1117. doi:10.1051/0004-6361:20034074
- Davies, B., Kudritzki, R.-P., Lardo, C., et al. 2017, *ApJ*, 847, 112. doi:10.3847/1538-4357/aa89ed
- De Somma, G., Marconi, M., Cassisi, S., et al. 2021, *MNRAS*. doi:10.1093/mnras/stab2611
- Efstathiou, G. 2020, arXiv:2007.10716
- Fitzpatrick, E. L. 1999, *PASP*, 111, 63. doi:10.1086/316293
- Freedman, W. L. & Madore, B. F. 2011, *ApJ*, 734, 46. doi:10.1088/0004-637X/734/1/46
- Freudling, W., Romaniello, M., Bramich, D. M., et al. 2013, *A&A*, 559, A96. doi:10.1051/0004-6361/201322494
- Genovali, K., Lemasle, B., Bono, G., et al. 2013, *A&A*, 554, A132. doi:10.1051/0004-6361/201321650
- Genovali, K., Lemasle, B., Bono, G., et al. 2014, *A&A*, 566, A37. doi:10.1051/0004-6361/201323198
- Kewley, L. J. & Ellison, S. L. 2008, *ApJ*, 681, 1183. doi:10.1086/587500
- Kovtyukh, V. V. & Gorlova, N. I. 2000, *A&A*, 358, 587.
- Leavitt, H. S. & Pickering, E. C. 1912, *Harvard College Observatory Circular*, 173
- Madore, B. F. 1982, *ApJ*, 253, 575. doi:10.1086/159659
- Møller Larsen, J., Modigliani, A. & Bramich, D. 2020, *UVES Pipeline Manual*, VLT-MAN-ESO-19500-2965, <ftp://ftp.eso.org/pub/dfs/pipelines/instruments/uves/uves-pipeline-manual-6.1.3.pdf>
- Mucciarelli, A. 2013, arXiv:1311.1403.
- Mucciarelli, A., Pancino, E., Lovisi, L., et al. 2013, *ApJ*, 766, 78. doi:10.1088/0004-637X/766/2/78
- Mucciarelli, A. & Bonifacio, P. 2020, *A&A*, 640, A87. doi:10.1051/0004-6361/202037703
- Mucciarelli, A. 2021, in preparation.
- Persson, S. E., Madore, B. F., Krzemiński, W., et al. 2004, *AJ*, 128, 2239. doi:10.1086/424934
- Planck Collaboration, Aghanim, N., Akrami, Y., et al. 2020, *A&A*, 641, A6. doi:10.1051/0004-6361/201833910
- Press, W. H. & Teukolsky, S. A. 1992, *Computers in Physics*, 6, 274
- Riess, A. G., Macri, L. M., Hoffmann, S. L., et al. 2016, *ApJ*, 826, 56. doi:10.3847/0004-637X/826/1/56
- Riess, A. G., Casertano, S., Yuan, W., et al. 2019, *ApJ*, 876, 85. doi:10.3847/1538-4357/ab1422
- Riess, A. G. 2020, *Nature Reviews Physics*, 2, 10. doi:10.1038/s42254-019-0137-0
- Riess, A. G., Casertano, S., Yuan, W., et al. 2021, *ApJ*, 908, L6. doi:10.3847/2041-8213/abdbaf
- Ripepi, V., Catanzaro, G., Molinaro, R., et al. 2021, *MNRAS*. doi:10.1093/mnras/stab2460
- Romaniello, M., Primas, F., Mottini, M., et al. 2008, *A&A*, 488, 731. doi:10.1051/0004-6361:20065661
- Sbordone, L. & Ledoux, C. 2020, *UVES Calibration Plan*, VLT-PLA-ESO-13200-1123, https://www.eso.org/sci/facilities/paranal/instruments/uves/doc/VLT-PLA-ESO-13200-1123_v106.pdf.
- Soszyński, I., Udalski, A., Szymański, M. K., et al. 2015, *Acta Astron.*, 65, 297
- Stetson, P. B. & Pancino, E. 2008, *PASP*, 120, 1332. doi:10.1086/596126
- Udalski, A., Szymański, M. K., & Szymański, G. 2015, *Acta Astron.*, 65, 1.
- Urbaneja, M. A., Kudritzki, R.-P., Gieren, W., et al. 2017, *AJ*, 154, 102. doi:10.3847/1538-3881/aa79a8
- Verde, L., Treu, T., & Riess, A. G. 2019, *Nature Astronomy*, 3, 891. doi:10.1038/s41550-019-0902-0

Appendix A: GALA configuration file

The full set of parameters we have used in the abundance analysis with GALA is included below, in the form of the input GALA file autofl.param. The reader is referred to the software documentation, specifically to the cookbook that comes with the software itself, for their definition and use.

```
# Parameter configuration file for GALA
# file created 2018/ 1/17 13:55
```

```
#-----#
#                                     BASIC PARAMETERS                                     #
#-----#

#----- OPTIMIZATION -----#
model      atlas9  # model atmospheres (atlas9,marcs...)
guess      5       # guess working block: 0 (disabled), 1 (enabled)
refine     1       # refine working block: 0 (disabled), 1 (enabled)
uncer      2       # uncertainties: 0 (disabled), 1 (Cayrel), 2 (Cayrel + trad.)
qiron      26.00   # code of the element used for the optimization
epot       1       # option for Teff optimization (0/1)
grc        1       # option for logg optimization (0/1/2/3)
vtc        1       # option for vturb optimization (0/1)
metal      1       # option for [M/H] optimization (0/1)
stepgr     0.1     # step of logg
stepteff   30      # step of Teff (K)
stepvt     0.1     # step of vturb (km/s)
iter       20      # number of iterations

#----- EW SELECTION -----#
ewstuff    no      # with * reads the following 3 parameters from 'list_star'
ewmin      -5.6    # minimum log(EW/lambda)
ewmax      -4.5    # maximum log(EW/lambda)
error      15      # maximum allowed EW error (in percentage)

#-----#
#                                     SUBORDINATE PARAMETERS                               #
#-----#

#----- REJECTION -----#
rj         1       # sigma-rejection from mean (0) or median (1)
smax       3       # number of sigma used in the line rejection
minl       3       # minimum number of lines to perform the line-rejection
minnfe     10      # minimum number of lines to perform the optimization
eplever    1.5     # minimum E.P. range to optimize Teff
maxsig     1.0     # maximum abundance dispersion to perform the optimization
minl       3       # minimum number of lines to perform the line rejection
errfit     1       # linear fits without errors (0), errors in y (1), in x and y (2)
paropt     0       # optimize Teff/vturb with slope (0) or Spearman coeff.(1)

#----- ADVANCED OPTIONS -----#
kuriter    5       # number of blocks of 15 iterations to calculate ATLAS9 models
inverse    -1      # values >= 0 enable the inverse analysis to derive new log(gf)
int_odf    1       # values >= 0 enable the interpolation in [M/H] for ATLAS9 ODFs

#----- OUTPUT -----#
plot       1       # produce (1) or not (0) the output plots
verbose    3       # verbosity level (from 0 to 3)
interz     0       # enable (1) or not (0) the interpolation to the zero value
```

```
debug      0      # remove (0) or not (1) temporary files
save       1      # save (1) or not (0) the new model atmospheres
cog        1      # calculate (1) or not (0) the curve of growth for all the lines
```

Appendix B: Input Equivalent Widths

We report here the detailed input to our abundance analysis. For each programme star, a file contains contain, in a format suitable for GALA, the Equivalent Widths of the individual spectral lines we have measured on the spectra with the DAOSPEC software, as well as the corresponding atomic physics.